larger than kilometer-size, which have negligible radial drift. Therefore, H_2O enrichments in the inner disk would be expected before the appearance of kilometer-size bodies in the outer disk.
34. J. N. Cuzzi, K. J. Zahnle, *Astrophys. J.*, in press.
35. Recently, UV dissociation of CO at high altitudes in the disk has been numerically estimated (*42*). Lyons and Young assume H_2O ice as a carrier of the ^{16}O-poor oxygen formed by their photodissociation process to generate ^{16}O-poor gas in the disk midplane similar to an idea that we had presented in our preliminary study (*22*). However, the degree of fractionation by the disk photochemistry is dependent on many unconstrained factors, including far-UV flux, the intensity of vertical eddy mixing, and the efficiency of H_2O formation. A more detailed study coupled with disk dynamics is needed to evaluate the contribution of their CO dissociation at high altitudes in the disk to oxygen isotopic heterogeneity observed in the solar system.
36. The bulk differences in oxygen isotopic composition observed among the meteorite groups and planets (*1*) could be explained by accretion at different times or by the incorporation of different amounts of nonvaporized water ice and solids with different degrees of the solid-gas equilibration. The solid-gas equilibration and the evolution of oxygen isotopic compositions of the gas in the inner region of the disk may have been recorded by refractory inclusions and chondrules in primitive meteorites.
37. S. Kurtz, R. Cesaroni, E. Churchwell, P. Hofner, C. M. Walmsley, in *Protostars and Planets IV*, V. Mannings, A. P. Boss, S. S. Russell, Eds. (Univ. of Arizona Press, Tucson, 2000), pp. 299–326.
38. W. D. Langer *et al.*, in *Protostars and Planets IV*, V. Mannings, A. P. Boss, S. S. Russell, Eds. (Univ. of Arizona Press, Tucson, 2000), pp. 29–57.
39. We use this value according to the traditional ^{16}O-enrichment observed in most Ca-A1–rich inclusions (*1*). Recently, a chondrule having twice the traditional enrichment ($\delta^{17 \text{ and } 18}O_{SMOW}$ of about –75‰) has been reported (*2*). Although such chondrules are rare, its least fractionated bulk chemical composition from the solar abundance suggests that the average oxygen isotopic composition of silicate in the solar system was originally more enriched in ^{16}O than the traditional value. According to our model, such an extreme ^{16}O-rich chondrule is interpreted as a closer representation of the pristine solar nebula value, implying that the ordinary refractory inclusions are no longer representative of the bulk solar nebula but moderately reprocessed by the interaction with the ^{17}O- and ^{18}O-rich H_2O.
40. N. Calvet, L. Hartmann, S. E. Strom, in *Protostars and Planets IV*, V. Mannings, A. P. Boss, S. S. Russell, Eds. (Univ. of Arizona Press, Tucson, 2000), pp. 377–399.
41. C. Hayashi, K. Nakazawa, Y. Nakagawa, in *Protostars and Protoplanets II*, D. C. Black, M. S. Matthews, Eds. (Univ. of Arizona Press, Tucson, 1985), pp. 1100–1153.
42. J. R. Lyons, E. D. Young, *Lunar Planet. Sci.* **35**, 1970 (2004).
43. We thank T. J. Fagan, A. N. Krot, and E. R. D. Scott for helpful discussion and improvement of the English and two anonymous reviewers for helpful comments. Supported by Monbu-Kagaku-sho grants.

2 June 2004; accepted 2 August 2004

Middle Miocene Southern Ocean Cooling and Antarctic Cryosphere Expansion

Amelia E. Shevenell,* James P. Kennett, David W. Lea

Magnesium/calcium data from Southern Ocean planktonic foraminifera demonstrate that high-latitude (~55°S) southwest Pacific sea surface temperatures (SSTs) cooled 6° to 7°C during the middle Miocene climate transition (14.2 to 13.8 million years ago). Stepwise surface cooling is paced by eccentricity forcing and precedes Antarctic cryosphere expansion by ~60 thousand years, suggesting the involvement of additional feedbacks during this interval of inferred low-atmospheric partial pressure of CO_2 (pCO_2). Comparing SSTs and global carbon cycling proxies challenges the notion that episodic pCO_2 drawdown drove this major Cenozoic climate transition. SST, salinity, and ice-volume trends suggest instead that orbitally paced ocean circulation changes altered meridional heat/vapor transport, triggering ice growth and global cooling.

The middle Miocene climate transition (MMCT), 14.2 to 13.8 million years ago (Ma), is one of the three major steps in Earth's Cenozoic climate evolution (*1–3*). The ~1‰ increase in the oxygen-isotopic composition ($\delta^{18}O$) of benthic foraminifera describes a combination of Antarctic ice growth and global cooling at ~14 Ma, as is also indicated by Southern Ocean ice-rafted detritus, eustatic change, and the fossil record (*1–6*). However, because $\delta^{18}O$ records both temperature and global ice volume, fundamental questions and uncertainties exist concerning the magnitude and phasing of middle Miocene ice growth and cooling. The development of Mg/Ca, an independent paleotemperature proxy measured on the same foraminiferal calcite ($CaCO_3$) as $\delta^{18}O$, has facilitated isolation of the ice-volume component of $\delta^{18}O$ records (*7–12*). The Mg/Ca content of foraminifera increases exponentially with temperature (~9 ± 1% per 1°C) and is relatively insensitive to salinity and ice-volume fluctuations (*7*, *8*). Low-resolution paired benthic foraminifer Mg/Ca and $\delta^{18}O$ studies designed to constrain the timing and magnitude of pre-Quaternary ice-volume fluctuations suggest substantial Antarctic ice growth (~0.85‰) and a concomitant deep ocean cooling (2°C to 3°C) during the MMCT (*11*, *12*). The magnitude of Antarctic ice growth and rapidity of this climate transition [<0.5 million years (My)] suggests that Earth's climate system was highly sensitive to oceanic, atmospheric, and cryospheric feedbacks.

Ocean circulation and atmospheric pCO_2 variations are often cited as potential catalysts of the MMCT (*13–17*). Large-scale reorganizations of ocean circulation driven by atmospheric circulation changes and/or tectonic reorganizations of gateway regions may have altered poleward heat and moisture transport, resulting in Antarctic ice growth and global cooling (*13–15*). Ocean circulation hypotheses are supported by $\delta^{13}C$ proxy evidence (*14*, *15*, *18*, *19*) and the timing of tectonic events in the eastern Tethys/Indonesia (*4*, *20*) and the North Atlantic (*13*). Alternatively, atmospheric pCO_2 drawdown, through organic carbon sequestration on the mid-latitude continental margins (*16*) and/or enhanced silicate weathering rates (*17*), may have driven Antarctic ice-sheet expansion and cooling at ~14 Ma. Support for this "Monterey Hypothesis" comes from thick, organic carbon-rich Miocene sedimentary sequences around the Pacific Rim (*4*, *16*) and a corresponding ~ 1‰ increase in global deep sea $\delta^{13}C$ (*4*, *16*, *21*, *22*). A potential complication of the hypothesis is revealed by paleo-pCO_2 estimates (*23–25*), which indicate that atmospheric pCO_2 levels declined >3 My before the MMCT and provide little support for either elevated atmospheric pCO_2 during the warm Miocene climatic optimum (MCO) (17 to 14 Ma) or a semipermanent atmospheric pCO_2 decrease at the MMCT. These estimates indicate that factors other than those related to global carbon cycling may contribute to this major Cenozoic climate transition. To evaluate the processes and feedbacks involved in the MMCT, detailed information is needed regarding the phasing of carbon cycling, Antarctic ice growth, and high-latitude oceanic/atmospheric cooling. Acquiring this information has thus far proven difficult because of the limited availability of $CaCO_3$-rich Southern Ocean sediments and the lack of an unambiguous paleotemperature proxy.

Here, we present an independent record of middle Miocene high-latitude Southern Ocean sea surface temperature (SST). To establish the thermal and hydrographic response of Southern Ocean surface waters and the phasing of high-latitude SST change, Antarctic cryosphere expansion, and global carbon cycling between ~17 and 13 Ma, we

Department of Geological Sciences and Marine Science Institute, University of California, Santa Barbara, CA 93106–9630, USA

*To whom correspondence should be addressed. E-mail: ashevenell@umail.ucsb.edu

generated paired Mg/Ca and $\delta^{18}O$ records from surface dwelling planktonic foraminifer *Globigerina bulloides* in conjunction with benthic foraminifer (*Cibicidoides mundulus*) $\delta^{18}O$ and $\delta^{13}C$ records at Ocean Drilling Program (ODP) Holes 1170A (47°90'S, 146°02.98'E; 2704 m) and 1171C (48°30'S, 149°06.69'E; 2150 m) on the South Tasman Rise (STR) (*26*) (Fig. 1). Plate tectonic reconstructions indicate that Sites 1170 and 1171 were situated at ~55°S in the middle Miocene (*27*), with calculated paleodepths of 2100 m and 1600 m, respectively (*28*). We used *G. bulloides* for several reasons. First, a well-defined modern subantarctic *G. bulloides* Mg-temperature calibration exists (*7*). Second, previous studies demonstrate the utility of *G. bulloides* Mg/Ca in reconstructing Quaternary subantarctic SSTs (*7*, *9*). Finally, *G. bulloides* is continuously present through both STR middle Miocene sequences (*26*). Hole 1171C Miocene *G. bulloides* Mg/Ca ranges between ~1.7 and 4.3 mmol/mol (Fig. 2 and table S1); minimum Mg/Ca values are similar to those from subantarctic core tops (*7*, *9*). The main feature of the *G. bulloides* Mg/Ca record is the 1.8 mmol/mol point-to-point decrease centered at 166.4 m below sea floor (mbsf) that marks the transition from relatively high to relatively low Mg/Ca. Three step-like features are superimposed on this transition (Fig. 2). Hole 1171C *G. bulloides* $\delta^{18}O$ ranges between ~0.0‰ and ~1.8‰ (*29*) (Fig. 2 and table S1). The main feature of the *G. bulloides* $\delta^{18}O$ record is the 0.9‰ point-to-point increase centered at 165.6 mbsf that marks the transition to more positive $\delta^{18}O$ values. The step-like structure of the Mg/Ca transition does not appear in the *G. bulloides* $\delta^{18}O$ record, which reflects ice volume and salinity influences in addition to temperature.

Diagenesis and dissolution may potentially alter the primary Mg/Ca signal encoded in planktonic foraminiferal calcite and, thus, the inferred SST record (*8*–*11*) (SOM Text). Several lines of evidence suggest that these processes have not biased our STR middle Miocene Mg/Ca values: (i) *G. bulloides* ultrastructures are visible, and shells do not exhibit extensive pitting, fragmentation, infilling, or overgrowth; (ii) the average $CaCO_3$ content of the middle Miocene ooze is stable at ~94% by weight (*26*) as a result of the intermediate STR paleodepths (*28*); and (iii) benthic and planktonic foraminifers exhibit interspecific $\delta^{18}O$ and $\delta^{13}C$ offsets (*30*).

We converted STR *G. bulloides* Mg/Ca values to temperatures using the calibration of Mashiotta *et al*. (*7*): SST = ln(Mg/Ca/0.474)/0.107 (SE, ±0.8°C). This calibration successfully estimates subantarctic Pacific (45°S to 56°S) and Indian Ocean (43°S) austral spring SSTs in both the modern and Quaternary (*7*, *9*). As ours is the first pre-Quaternary study employing this calibration, we assume that the environmental preferences of middle Miocene subantarctic *G. bulloides* and physical processes governing Mg uptake are similar to those in modern subantarctic *G. bulloides*. These processes and seawater Mg/Ca (*31*) may have changed through time and could contribute an additional uncertainty of up to 3°C in the conversion of Mg/Ca to absolute temperature (SOM Text). However, this uncertainty would not affect the magnitude of inferred temperature shifts on time scales <1 My. Age models derived from magnetostratigraphy, biostratigraphy, and stable isotope datums (*32*) provide the chronologic framework for the STR records (SOM Text).

Mg/Ca evidence from Hole 1171C indicates that regional SSTs were ~2°C cooler after ~14 Ma (14.7 ± 1.1°C; 13.9 to 12 Ma) than during the preceding MCO (17.0 ± 1.2°C; 17 to 14 Ma) (Fig. 3) (*3*, *4*). Paleobotanical and faunal paleotemperature estimates from southern Australia and New Zealand support this trend and are similar to, or slightly cooler than, *G. bulloides* Mg/Ca-derived SST estimates (*4*, *33*). The major feature of the STR SST record is a ~7°C (point-to-point) transition (14.2 to 13.9 Ma) from the warmest MCO to cooler post-MMCT SSTs

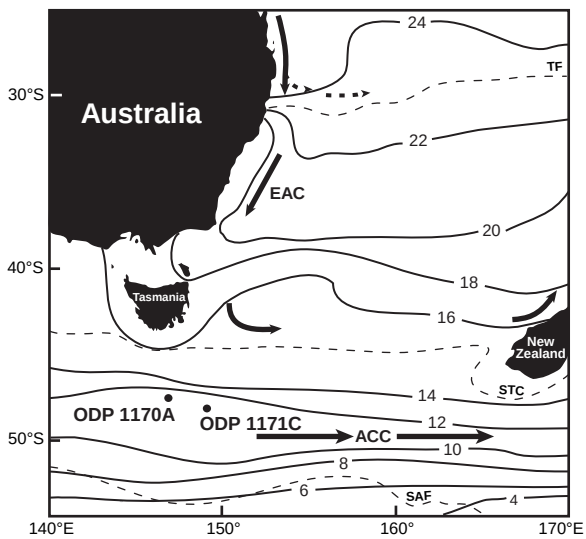

Fig. 1. Annual average SSTs in the subantarctic southwest Pacific (*39*) with Ocean Drilling Program (ODP) South Tasman Rise (STR) sites indicated. ODP Site 1171 is located at the intersection of the southward-flowing East Australian Current (EAC) and the eastward-flowing Antarctic Circumpolar Current (ACC), one of three locations where heat is introduced to the Southern Ocean (*26*). ODP Site 1170 is located 50 km northwest of Site 1171, beyond the influence of the EAC (*26*). In the middle Miocene, the STR was situated at ~55°S, 5° to 7° south of its present location (*27*). Backtracked middle Miocene paleodepths of Sites 1170 and 1171 are 2100 m and 1600 m, respectively (*28*). Currently, STR hydrography is controlled by the Subtropical Convergence (STC) to the north and the Subantarctic Front (SAF) to the south. Seasonal SST variation is ~4°C (*26*, *39*). *G. bulloides* calcifies in the mixed layer during the austral spring when regional surface temperatures range between 8°C and 12°C (*9*, *39*).

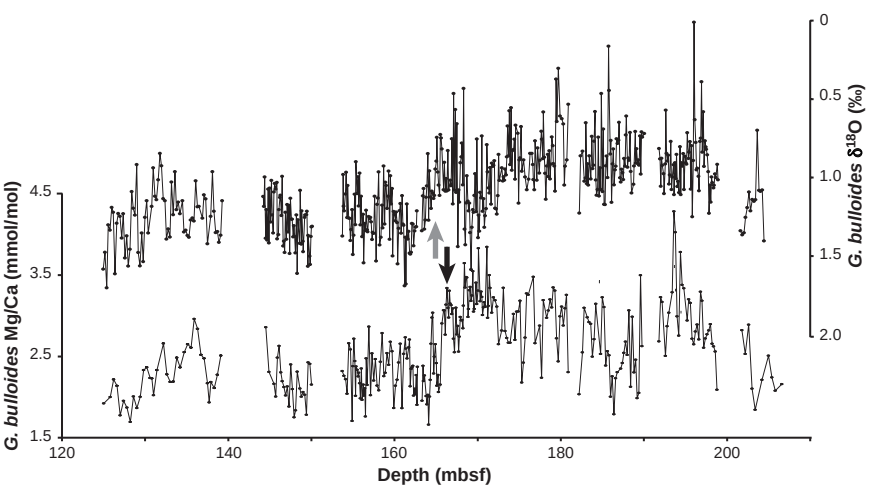

Fig. 2. Climate proxy data from South Tasman Rise (STR) ODP Hole 1171C (48°30'S, 149°06.69'E; 2150 m). The Mg/Ca record was generated on planktonic foraminifer species *G. bulloides* at 20-cm intervals from 125 to 154 mbsf and from 154 to 207 mbsf and at 10-cm intervals between 154 and 172 mbsf. Each point represents an average of one to four analyses; pooled SD of all replicates (df = 64) is ±0.21 mmol/mol (±7.8%). Measured modern southwest Pacific core top Mg/Ca is ~1.6 mmol/mol (*9*). Oxygen isotope ($\delta^{18}O$) data were generated from *G. bulloides* at 10-cm intervals between 125 and 207 mbsf. The black arrow denotes the midpoint of the major 1.8 mmol/mol Mg/Ca transition, and the gray arrow denotes the midpoint of the 0.9‰ *G. bulloides* $\delta^{18}O$ transition. Gaps in the data are due to incomplete core recovery (*26*).

(Fig. 3). Inferred orbital-scale [~400 and 100 thousand years (ky)] SST variability is particularly pronounced during the MMCT. Cooling occurred in three distinct steps (midpoints, 14.2, 14.0, and 13.9 Ma) and was followed by an interval of relatively cold SSTs (13.7 ± 1.1°C; 13.9 to 13.8 Ma) (Figs. 3 and 4). At ~13.8 Ma, regional SSTs warm by ~2°C to 3°C and remain relatively stable until ~12 Ma. We confirmed the Hole 1171C SST estimates by measuring *G. bulloides* Mg/Ca at a second STR location, Hole 1170A [~54°S (*27*); 2100 m (*28*)] (Figs. 1 and 3, table S2), with a different depositional history (*26*). Similarities in both magnitude (±0.5°C) and structure of the two records (Fig. 3) further support our interpretation of STR *G. bulloides* Mg/Ca as a primary climate signal. We attribute several offsets between the records to age model and sampling resolution differences (*30*) (SOM Text).

Large-amplitude SST fluctuations over the STR suggest substantial reorganization of Southern Ocean surface waters during the MMCT. One possible explanation is an orbitally paced intensification of the Antarctic Circumpolar Current (ACC) system, perhaps related to increased westerly wind strength. This idea is supported by a paleobotanic record of regional wind strength (*4*, *34*), substantial evidence for increased meridional thermal gradients (*4*), the timing of major Southern Ocean unconformities (*4*, *5*), and STR surface water $\delta^{18}O$ ($\delta^{18}O_w$). We used Hole 1171C *G. bulloides* Mg/Ca SST and $\delta^{18}O$ (table S1) to calculate $\delta^{18}O_w$ (*7*, *8*) (SOM Text) (fig. S1), which should reflect some combination of ice volume and local salinity effects. Large SST fluctuations during the MMCT obscure the *G. bulloides* $\delta^{18}O$ increase, which indicates that STR $\delta^{18}O_w$ likely reflects regional salinity variations. Strict interpretation of the $\delta^{18}O_w$ results suggests a gradual freshening of regional surface waters between 14.2 and 13.8 Ma, consistent with enhanced ACC strength and the resultant increased influence of subantarctic surface waters over the STR. A notably similar pattern of oceanographic change is recognized in the southwest Pacific during Quaternary glaciations (*9*, *35*).

Orbital-scale cyclicity (400 and 100 ky) is inferred in the STR records of *G. bulloides* Mg/Ca and *C. mundulus* $\delta^{18}O$ and $\delta^{13}C$. This cyclicity indicates a potential role for Milankovitch forcing during the MMCT, which suggests that Earth's climate system was particularly sensitive to forcing at eccentricity frequencies between ~15 and 13.5 Ma. Comparison of orbital curves (*36*) to untuned STR SST and *C. mundulus* $\delta^{18}O$, an ice-volume proxy (*32*) (SOM Text), reveals that the MMCT occurred within an interval of high obliquity and moderate eccentricity variance (Fig. 4) (*36*). This relationship suggests that, at 14.2 Ma, Antarctic ice sheets were large enough to survive warm summer orbital configurations but small enough to respond dynamically to orbital forcing (*37*). Surface cooling generally corresponds with long-period (~400 ky) eccentricity minima between 14.2 and 13.8 Ma (which are similar in amplitude to previous and subsequent minima) and precedes Antarctic ice growth by ~60 ky (as judged by the midpoints of the major Mg/Ca and *C. mundulus* $\delta^{18}O$ transitions). Our data suggest that orbital forcing paced both Southern Ocean SSTs and Antarctic ice growth during the MMCT. There is, however, no obvious orbital anomaly akin to that recognized at the Oligocene/Miocene boundary (*38*), and, assuming a synchronous atmospheric and SST response, the substantial time lag (~60 ky) between orbital forcing and ice growth supports the notion that additional feedbacks (e.g., carbon cycling, ocean circulation, and/or ice/albedo feedbacks) may be required for substantial and rapid Antarctic ice growth. Heightened sensitivity to eccentricity forcing between 14.2 and 13.8 Ma and the phasing of SST and ice volume ($\delta^{18}O$) are clues to identifying the feedbacks involved in this climate threshold.

Model results stress a fundamental role for atmospheric pCO_2 in Cenozoic climate change and indicate that the Antarctic cryosphere may react sensitively to climate feedbacks only when atmospheric pCO_2 is relatively low and within some narrowly defined

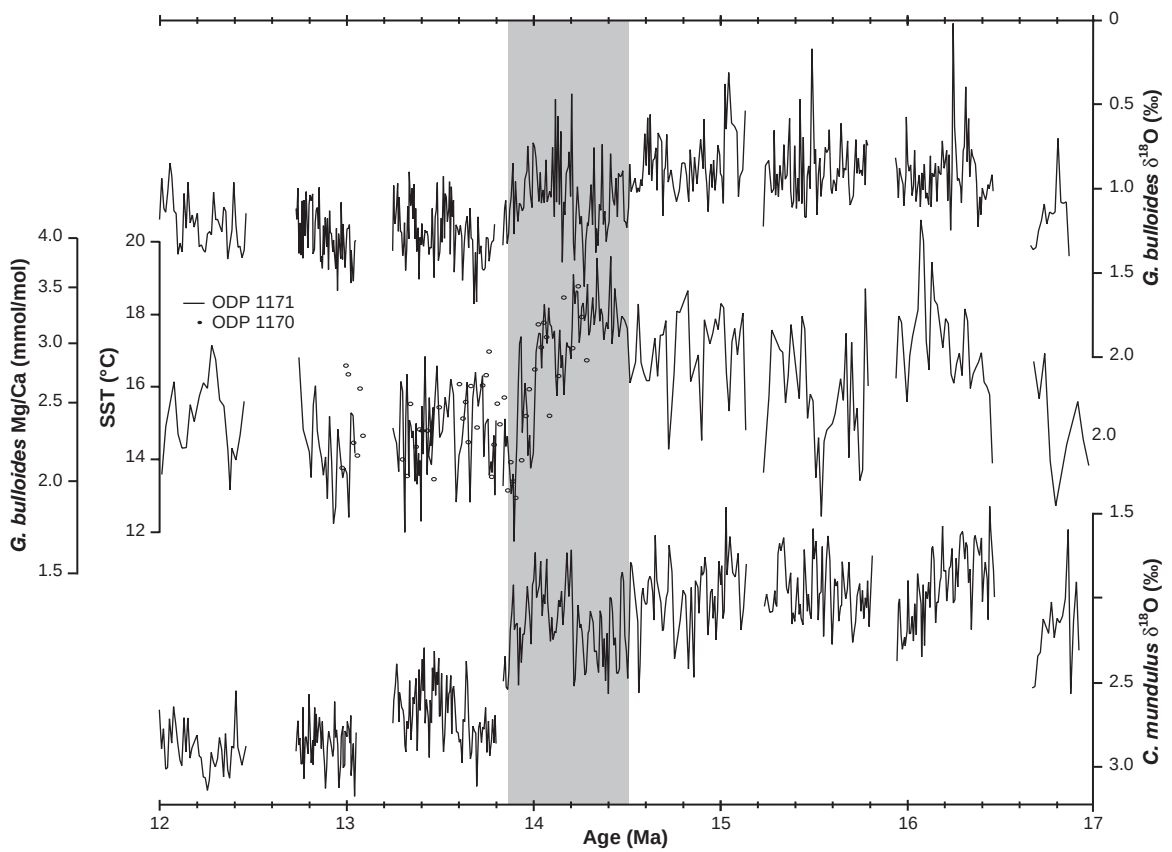

Fig. 3. Hole 1171C middle Miocene (12 to 17 Ma) *G. bulloides* $\delta^{18}O$, SST, and benthic foraminifer (*C. mundulus*) $\delta^{18}O$ (*32*) records versus age. Mg/Ca–derived SSTs from Hole 1170A (open circles) are plotted with the Site 1170 age model. Age models at Sites 1170 and 1171 were constructed using magnetostratigraphy, biostratigraphy, and stable isotope datums (*26*, *32*). The *G. bulloides* Mg/Ca values were converted to SST by using the equation of Mashiotta *et al*. (*7*). Both the Mg/Ca and SST scales are given. The *C. mundulus* $\delta^{18}O$ record serves as a general proxy for Antarctic ice volume (*11*, *30*) (SOM Text).

range (*37*). Sensitivity to eccentricity forcing is apparent in many middle Miocene $\delta^{13}C$ records between 17 and 13.5 Ma (*4*, *14*, *15*, *18*, *21*, *22*), which suggests at least some role for the carbon cycle in the MMCT. However, the >3 My discrepancy between the initial atmospheric pCO_2 decline (*23*, *24*) and the MMCT has shifted focus to the role of episodic pCO_2 drawdown, associated with more positive $\delta^{13}C$ carbon maxima (CM) events, in triggering this major climate step (*21*). Moderate resolution records suggest that CM events, which are attributed to climate-induced variations in marine organic carbon sequestration, co-vary with analogous $\delta^{18}O$ events at the 400-ky frequency (*14*, *15*, *18*). Comparison of STR *G. bulloides* Mg/Ca to *C. mundulus* $\delta^{18}O$ (ice volume) and $\delta^{13}C$, a general proxy for carbon cycling and atmospheric pCO_2, reveals that Southern Ocean surface-water cooling and Antarctic ice growth occurred between CM5 and CM6 during an interval of increasing pCO_2 (Fig. 4) (*23*). This sequence of change challenges the notion that episodic pCO_2 drawdown was the primary forcing that triggered the MMCT, again implying that other feedbacks (e.g., ice/albedo) played a more significant role in this climate transition. Our records also indicate that CM6, one of the largest CM events, corresponds with maximum Antarctic ice volume and a slight warming of the high southern latitudes. This relationship raises the possibility that feedbacks related to Antarctic cryosphere expansion may have exerted control over the global carbon cycle through enhanced ventilation of intermediate and deep ocean waters and falling sea levels (*4*, *6*, *23*). The long-term trend observed in the global $\delta^{13}C$ record after the rapid expansion of Antarctic ice volume supports this interpretation (*3*).

Our results demonstrate that STR SSTs cooled 6°C to 7°C between 14.2 and 13.8 Ma, revealing that the Southern Ocean was a dynamic component of the MMCT. Eccentricity-paced Southern Ocean surface cooling and freshening suggest that atmospheric/oceanic circumpolar circulation intensified in response to orbital forcing, increasingly thermally isolating Antarctica during the MMCT (14.2 to13.8 Ma). Middle Miocene intensification of the ACC may have played a major role in Cenozoic climate evolution, both directly through changes in meridional heat transport and indirectly through changes in vapor transport. We speculate that sensitivity to eccentricity forcing increased at 14.2 Ma, immediately following peak warmth of the MCO (*23–25*) as a result both of low atmospheric pCO_2 (*37*) and of a fundamental reorganization of the climate system, specifically a tectonically mediated reduction in meridional heat/vapor transport related to the constriction of the Eastern Tethys at ~15 Ma (*4*, *14*, *20*). The presence of 100-ky variability (14.2 to 13.8 Ma) and a rare shift in eccentricity cadence between 15 and 14 Ma (*36*) are intriguing, and future efforts should focus on understanding the evolution of the climate spectrum on orbital time scales during the MMCT.

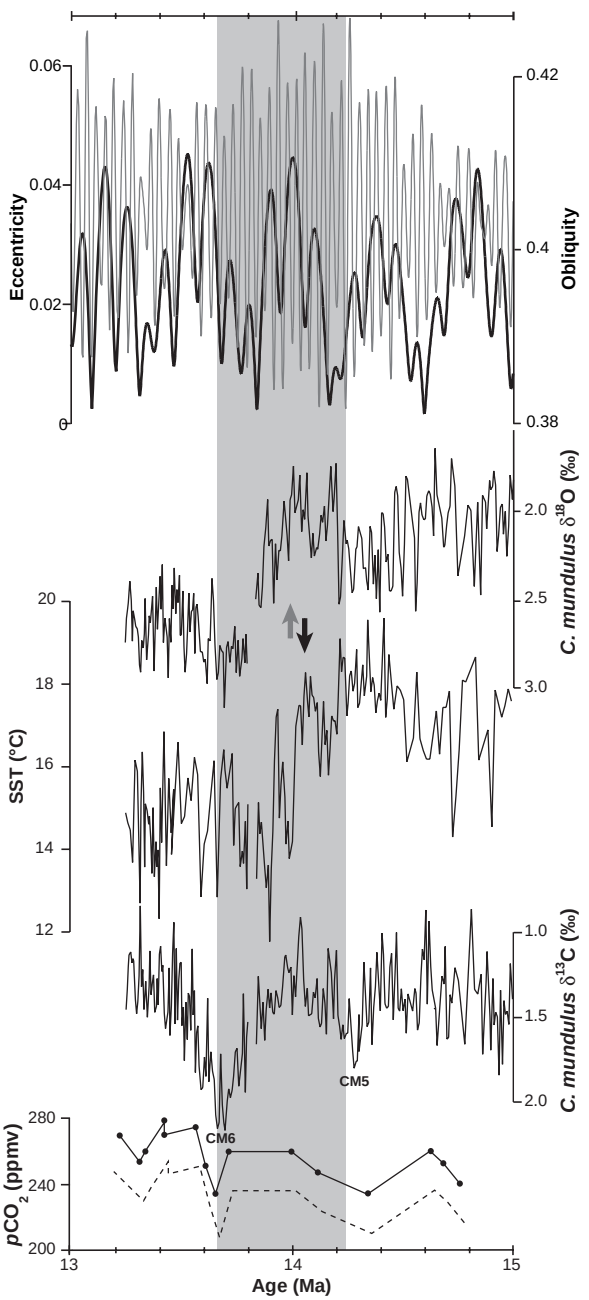

Fig. 4. Expanded view of the 13- to 15-Ma interval. Site 1171 SSTs are compared with *C. mundulus* $\delta^{18}O$ and $\delta^{13}C$ records (*32*). Orbital solutions (*36*) are plotted; eccentricity (black) and obliquity (gray). Paleo-pCO_2 estimates derived from southwest Pacific alkenone $\delta^{13}C$ (*23*); maximum (solid line) and minimum (dashed line) estimates are plotted. All records are plotted on the Site 1171 age scale (*32*) (SOM Text). Midpoints of the SST and *C. mundulus* $\delta^{18}O$ transitions are 14.07 Ma (black arrow) and 14.01 Ma (gray arrow), respectively. The final $\delta^{13}C$ increase of the "Monterey" $\delta^{13}C$ excursion (CM6) begins at 13.8 Ma and terminates at 13.6 Ma.

References and Notes

1. N. J. Shackleton, J. P. Kennett, in *Initial Reports of the Deep Sea Drilling Project* (U.S. Government Printing Office, Washington, DC, 1975), vol. 29, pp. 743–755.
2. K. G. Miller, R. G. Fairbanks, G. S. Mountain, *Paleoceanography* **2**, 1 (1987).
3. J. Zachos, M. Pagani, L. Sloan, E. Thomas, K. Billups, *Science* **292**, 686 (2001).
4. B. P. Flower, J. P. Kennett, *Palaeogeogr. Palaeoclimatol. Palaeoecol.* **108**, 537 (1994).
5. J. P. Kennett, P. F. Barker, *Proc. Ocean Drill. Program Sci. Results* **113**, 937 (1990).
6. B. U. Haq, J. Hardenbol, P. Vail, *Science* **235**, 1156 (1987).
7. T. A. Mashiotta, D. W. Lea, H. J. Spero, *Earth Planet. Sci. Lett.* **170**, 417 (1999).
8. D. W. Lea, D. K. Pak, H. J. Spero, *Science* **289**, 1719 (2000).
9. K. Pahnke, R. Zahn, H. Elderfield, M. Schulz, *Science* **301**, 948 (2003).
10. Y. Rosenthal, G. P. Lohmann, *Paleoceanography* **17**, 1044 (2002).
11. C. H. Lear, H. Elderfield, P. A. Wilson, *Science* **287**, 269 (2000).
12. K. Billups, D. P. Schrag, *Paleoceanography* **17**, 1003 (2002).
13. D. Schnitker, *Nature* **284**, 615 (1980).
14. F. Woodruff, S. M. Savin, *Paleoceanography* **4**, 87 (1989).
15. J. D. Wright, K. G. Miller, R. G. Fairbanks, *Paleoceanography* **7**, 357 (1992).
16. E. Vincent, W. H. Berger, in *The Carbon Cycle and Atmospheric CO_2: Natural Variations Archean to Present*, E. T. Sundquist, W. S. Broecker, Eds. (American Geophysical Union, Washington, DC, 1985), vol. 32, pp. 455–468.
17. M. E. Raymo, *Paleoceanography* **9**, 399 (1994).

18. B. F. Flower, J. P. Kennett, *Paleoceanography* **10**, 1095 (1995).
19. I. R. Hall *et al.*, *Paleoceanography* **18**, 1040 (2003).
20. K. J. Hsu, D. Bernoulli, in *Initial Reports of the Deep Sea Drilling Project* (U.S. Government Printing Office, Washington, DC, 1975), vol. 42, pp. 943–950.
21. B. F. Flower, J. P. Kennett, *Geology* **21**, 877 (1993).
22. D. A. Hodell, F. Woodruff, *Paleoceanography* **9**, 405 (1994).
23. M. Pagani, M. A. Arthur, K. H. Freeman, *Paleoceanography* **14**, 273 (1999).
24. P. N. Pearson, M. R. Palmer, *Nature* **406**, 695 (2000).
25. D. L. Royer *et al.*, *Science* **292**, 2310 (2001).
26. N. F. Exon *et al.*, *Proc. Ocean Drill. Prog., Init. Rep.* (Ocean Drilling Program, College Station, TX 2001), vol. 189.
27. L. A. Lawver, L. M. Gahagan, M. F. Coffin, in *The Antarctic Paleoenvironment: A Perspective on Global Change*, J. P. Kennett and D. A. Warnke, Eds. (American Geophysical Union, Washington, DC, 1992), pp. 7–30.
28. J. G. Sclater, L. Meinke, A. Bennett, C. Murphy, in *The Miocene Ocean: Paleoceanography and Biogeography*, J. P. Kennett, Ed. (The Geological Society of America, Boulder, CO 1985), pp. 1–21.
29. Materials and methods are available as supporting material on *Science* Online.
30. A. E. Shevenell, unpublished data.
31. B. Wilkinson, T. Algeo, *Am. J. Sci.* **289**, 1158 (1989).
32. A. E. Shevenell, J. P. Kennett, in *The Cenozoic Southern Ocean: Tectonics, sedimentation, and climate change between Australia and Antarctica*, N. F. Exon, J. P. Kennett, M. J. Malone, Eds. (American Geophysical Union, Washington, DC, in press).
33. I. R. K. Sluiter, A. P. Kershaw, G. R. Holdgate, D. Bulman, *Int. J. Coal Geol.* **28**, 277 (1995).
34. S. Locker, E. Martini, *Geol. Rundsch.* **78**, 1165 (1989).
35. F. Lamy *et al.*, *Science* **304**, 1959 (2004).
36. J. Laskar *et al.*, *Astron. Astrophys.*, in press.
37. R. M. DeConto, D. Pollard, *Nature* **421**, 245 (2003).
38. J. C. Zachos, N. J. Shackleton, J. S. Revanaugh, H. Pälike, B. P. Flower, *Science* **292**, 274 (2001).
39. S. R. Rintoul, J. L. Bullister, *Deep-Sea Res.* **46**, 1417 (1999).

40. Supported by NSF grant OPP0229898 to J. P. Kennett and JOI/USSSP postcruise funds to A. E. Shevenell. This research used samples provided by the Ocean Drilling Program. Mass spectrometer operation/support by G. Paradis and H. Berg and laboratory assistance from K. Thompson were critical to the success of this study. We thank the Gulf Coast Repository staff for providing samples; I. Hendy, M. Hommeyer, P. Martin, and D. Pak for discussion; and reviewers for suggestions.

Supporting Online Material
www.sciencemag.org/cgi/content/full/305/5691/1766/DC1
Materials and Methods
SOM Text
Fig. S1
Tables S1 and S2
References

7 May 2004; accepted 10 August 2004

Crystal Structure of a Shark Single-Domain Antibody V Region in Complex with Lysozyme

Robyn L. Stanfield,[1]* Helen Dooley,[3]* Martin F. Flajnik,[3] Ian A. Wilson[1,2]†

Cartilaginous fish are the phylogenetically oldest living organisms known to possess components of the vertebrate adaptive immune system. Key to their immune response are heavy-chain, homodimeric immunoglobulins called new antigen receptors (IgNARs), in which the variable (V) domains recognize antigens with only a single immunoglobulin domain, akin to camelid heavy-chain V domains. The 1.45 angstrom resolution crystal structure of the type I IgNAR V domain in complex with hen egg-white lysozyme (HEL) reveals a minimal antigen-binding domain that contains only two of the three conventional complementarity-determining regions but still binds HEL with nanomolar affinity by means of a binding interface comparable in size to conventional antibodies.

The cartilaginous fish (sharks, skates, rays, and chimeras) diverged from a common ancestor with other jawed vertebrates approximately 500 million years ago and include over 700 extant species. Nevertheless, they possess an adaptive immune system based on immunoglobulin (Ig), T cell receptors (TCRs), and the major histocompatibility complex. Three immunoglobulin isotypes have been identified in cartilaginous fish: two standard heavy (H)-light (L)-chain isotypes, designated IgM and IgW (IgW is also called IgX or IgNARC); and an atypical isotype, IgNAR. IgNAR is an H-chain homodimer that does not associate with L chain (*1*, *2*), unlike conventional human and murine antibodies (Fig. 1). Each H chain has one variable (V) and five constant (C) domains. Electron microscopy studies of IgNAR have revealed that their V regions are single domains, tethered to the C domains by means of flexible hinge-like regions (*2*). The V regions of IgNAR are not closely related to the V_H regions of either shark IgM or IgW in phylogenetic tree analyses; rather, they cluster with the V regions of TCR or immunoglobulin L chains (*1*, *3*).

In addition to the two canonical cysteines typical of immunoglobulin domains, IgNAR V domains carry a number of noncanonical cysteines that enable classification into two closely related subtypes, I and II. Type II V regions have an additional cysteine in complementarity-determining regions (CDRs) 1 and 3, which have been proposed to form a domain-constraining disulfide bond, akin to those observed in camelid H-chain V (V_HH) domains (*2*, *4*), whereas the extra cysteines in type I V regions are in framework regions (FRs) 2 and 4, and another two or four cysteines are

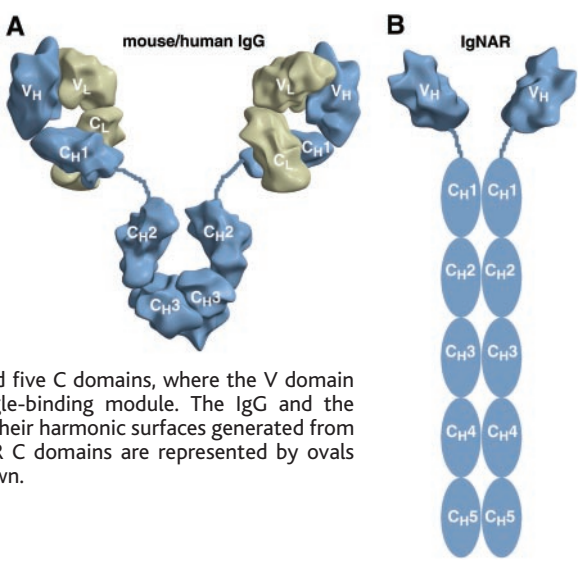

Fig. 1. Schematic representation of the overall IgG and IgNAR architectures. (**A**) A conventional IgG is composed of two H chains (blue) and two L chains (yellow) that assemble to form one Fc and two Fab regions or superdomains. The H chain has three C domains (C_H1, C_H2, and C_H3) and one V domain (V_H), whereas the L chain has one C domain (C_L) and one V domain (V_L). The V region is made up of two immunoglobulin domains (V_H and V_L). (**B**) IgNAR has only two H chains, each consisting of one V and five C domains, where the V domain is unpaired and constitutes a single-binding module. The IgG and the IgNAR domains are represented by their harmonic surfaces generated from atomic coordinates (*27*); the IgNAR C domains are represented by ovals because their structures are unknown.

[1]Department of Molecular Biology, [2]Skaggs Institute for Chemical Biology, The Scripps Research Institute, 10550 North Torrey Pines Road, La Jolla, CA 92037, USA. [3]Department of Microbiology and Immunology, University of Maryland at Baltimore, Baltimore, MD 21201–1559, USA, and the National Aquarium in Baltimore, 501 E. Pratt Street, Baltimore, MD 21202, USA.

*These authors contributed equally to this work.
†To whom correspondence should be addressed. E-mail: wilson@scripps.edu